Article

Not peer-reviewed version

Spatial and Temporal Study of the Post-Compressed High-Power Laser Pulses for Coherent Extreme Ultraviolet Source Development

Cong Zhou , Haina Wu * , Chaoneng Wu , Yitong Zhao , Chen Wang , Jiayue Liu , Zige Qiu , Wei Zhang , Yapei Peng , Mingyuan Shi , Shuyuan Hu , Xiaoliang Liu , Sizhong Wu , Jie Yang , Cangtao Zhou , Lu Li *

Posted Date: 22 April 2026

doi: 10.20944/preprints202604.1561.v1

Keywords: hollow-core fiber; multi-pass cell; post-compression; spatial quality; high harmonic generation

Preprints.org (www.preprints.org) | NOT PEER-REVIEWED | Posted: 22 April 2026 doi:10.20944/preprints202604.1561.v1

Article

Spatial and Temporal Study of the Post-Compressed High-Power Laser Pulses for Coherent Extreme Ultraviolet Source Development

Cong Zhou [1], Haina Wu [1,*], Chaoneng Wu [1], Yitong Zhao [1,2,3], Chen Wang [1], Jiayue Liu [1], Zige Qiu [1], Wei Zhang [1], Yapei Peng [1], Mingyuan Shi [1], Shuyuan Hu [1], Xiaoliang Liu [4], Sizhong Wu [1], Jie Yang [2,3], Cangtao Zhou [1] and Lu Li [1,*]

[1] Shenzhen Key Laboratory of Ultraintense Laser and Advanced Material Technology, College of Engineering Physics, and Center for Intense Laser Application Technology, Shenzhen Technology University, Shenzhen 518118, China
[2] Institute of Modern Physics, Chinese Academy of Sciences, Lanzhou 730000
[3] University of Chinese Academy of Sciences, Beijing 100049, China
[4] School of Nuclear Science and Engineering, East China University of Technology, Nanchang 330013, Jiangxi, China
* Correspondence: wuhaina@sztu.edu.cn, lilu@sztu.edu.cn

Abstract

Post-compression based on self-phase modulation (SPM) is widely used for femtosecond pulse shortening. However, the influence of the driving beam wavefront on different compression schemes remains unexplored. Using a Yb-doped fiber laser (230 fs, 200 kHz), we experimentally compare pulse compression in a hollow-core fiber (HCF) and a multi-pass cell (MPC). The HCF compresses pulses to 27 fs with an efficiency of approximately 55% and improves beam quality via modal filtering. The MPC achieves 34 fs pulses with an efficiency of approximately 90% and exhibits a quasi-waveguide mode-filtering effect, substantially enhancing output wavefront quality even when the input wavefront is poor. High-harmonic generation (HHG) experiments show that the HCF-driven source yields a higher photon flux (1.25×10^{11} photons/s) compared to the MPC-driven source (4.95×10^{10} photons/s). Using a second Yb-doped fiber laser (223 fs, 100 kHz), a cascaded MPC–HCF scheme generates 7.5 fs pulses with an overall efficiency of approximately 70%, enabled by employing a larger-core HCF in the second compression stage. HHG experiments performed with the compressed pulses demonstrate that spatial phase evolution is a critical parameter in post-compression design for such applications.

Keywords: hollow-core fiber; multi-pass cell; post-compression; spatial quality; high harmonic generation

---

1. Introduction

Since the invention of chirped-pulse amplification (CPA) technique [1], the peak power of ultrafast lasers has increased dramatically over the past four decades. High average and peak power are critical parameters for most applications in the ultrafast domain. Although Ti:Sapphire based systems, the current workhorse for high-power amplifiers, have achieved peak powers in the multi tens petawatt regime [2], they face fundamental limitations. The achievable pulse energy is constrained by nonlinear effects, such as self-phase modulation and self-focusing, which can degrade pulse quality and risk damaging the amplifier. Furthermore, the average power of Ti:Sapphire lasers is typically within 10W, primarily due to thermally induced wave front distortions, gain medium overheating, and the thermomechanical stability of the laser architecture.

To overcome these limitations, state-of-the-art high power laser systems are predominantly configured as solid-state laser sources based on the master oscillator power amplifier (MOPA) architecture, often incorporating CPA. Among these, ytterbium (Yb)-doped gain media have emerged as a leading technology, offering significantly higher average output power than conventional Ti:Sapphire lasers. Yb-based bulk crystal [3], disk [4], slab [5], fiber [6] lasers can now deliver ultrashort pulses with average powers exceeding hundreds of watts. Notably, the Yb-doped thin-disk laser has the potential to scale to tens of kilowatts [7], representing an improvement of two to three orders of magnitude over typical Ti:Sapphire systems. However, a key drawback of Yb-doped lasers is their limited gain bandwidth, which generally confines pulse durations to the hundred-femtosecond regime. Representative values are around 190 fs for Yb:KGW platforms (e.g., Light Conversion's PHAROS series) and approximately 500 fs for Yb:YAG systems (e.g., Trumpf's DIRA series).

The relatively long pulse duration of Yb lasers presents significant drawbacks compared to the sub 25 fs pulses from Ti:Sapphire systems, particularly for applications in materials processing, strong-field physics, and secondary source generation. For example, in high harmonic generation, longer pulses lead to lower conversion efficiencies due to exacerbated ionization-induced phase mismatch and restricted transient phase-matching conditions [8]. Lorek et al. demonstrated this challenge, achieving an HHG conversion efficiency of only 1.3×10^{-10} with an 800 fs fiber laser driver [9]. Consequently, post-compressing the high-power pulses from Yb lasers to shorter duration has become imperative for unlocking their full application potential, such as enhancing HHG efficiency for attosecond science.

Several post-compression techniques have been developed to this end, with the most prominent being HCF, Herriott-type MPC, and multi-thin-plates (MTP). The underlying principle of these methods relies on self-phase modulation (SPM) induced by the optical Kerr effect as the laser beam propagates through a nonlinear medium. The SPM process generates new frequency components, which are subsequently temporally compressed, typically using a set of chirped mirrors, to yield a shorter pulse. While HCF [10–12], MPC [13], MTP [14], and their cascades [15,16] have all demonstrated the ability to produce nearly single-cycle pulses, each of these schemes possesses distinct advantages and limitations. The MTP scheme, for instance, offers a compact footprint but often requires hybridization with other techniques to achieve high compression factors due to its lower nonlinearity per pass. Its average power handling is also restricted by the damage threshold of the solid plates, and it carries a risk of spatial degradation and nonlinear focusing at high powers. In contrast, HCF and MPC schemes generally offer superior peak and average power handling.

While significant progress has been made in improving temporal compression, the spatial properties of post-compressed beams—particularly wavefront quality—have received comparatively less attention. However, in phase-sensitive processes such as HHG, the spatial phase of the driving laser plays a critical role in determining phase-matching conditions, focal intensity distribution, and the coherence of the generated radiation. It is well established that wavefront aberrations can significantly degrade HHG efficiency by shortening the effective interaction length and disrupting the coherent buildup of harmonic emission [17]. Furthermore, the wavefront of the generated harmonics is strongly influenced by the wavefront of the driving infrared laser, enabling direct control of extreme ultraviolet (XUV) beam properties through manipulation of the input phase [18]. Accurate characterization of the harmonic wavefront is therefore essential for understanding the nonlinear interaction and optimizing applications such as attosecond metrology and coherent imaging [19]. In addition to externally imposed aberrations, the HHG process itself can introduce intrinsic spatiotemporal coupling and chromatic wavefront distortions, further complicating the overall beam quality [20]. These considerations highlight that precise control of the spatial phase of the driving laser is crucial for achieving efficient and high-quality HHG output [21].

In self-phase modulation based post compression systems, the spatial and temporal dynamics are intrinsically coupled. Waveguide-based approaches such as HCF provide modal filtering that suppresses higher-order spatial modes, whereas free-space multi-pass systems are more susceptible to cumulative aberrations introduced by optical components. However, a systematic comparison of these techniques from the perspective of spatial phase evolution remains limited.

In this work, we present a comprehensive investigation of the temporal, spectral, and spatial properties of post-compressed laser pulses using HCF and MPC schemes. By combining pulse characterization with wavefront phase measurements, we analyze the interplay between compression efficiency and beam quality, and further evaluate their impact on high harmonic generation.

2. Experimental Setup

Current experiments were carried out with a commercial high power (70W) Yb-doped fiber laser system, which provides maximum pulse energy $350\,\mu J$ and pulse duration ~230 fs at 200kHz repetition rate. As illustrated in Figure 1, the output beam firstly passes through an optical isolator (ISO) to prevent back-reflections into the laser system. A motorized energy attenuator consisting of a half-waveplate $(\lambda/2)$ and two thin film polarizers (TFP) is installed after the ISO for precise pulse energy control. Subsequently, a flexible beam expander and a focal lens $(f = 1m)$ are employed to ensure the correct beam waist coupled into the post-compression module.

Figures 1 and 2 show the experiment layout for HCF and MPC post-compression system, respectively. Two fine-tuning mirrors (M1 and M2) are crucial to accurately steer the beam into the post-compression module. For the HCF module, as it shown in Figure 1, the HCF system consist of a 1.35m-long capillary with an inner bore diameter of 250μm, a 2.5-meter-long vacuum chamber equipped with two Brewster windows (made of fused silica, polished to $\lambda/10$ surface quality, with a thickness of 2mm ±0.2mm) and a set of chirped mirrors. Benefiting from high ionization potential and large nonlinearity, argon gas was chosen to fill into the capillary to induce sufficient spectral broadening via SPM process while minimizing plasma-induced losses. To optimize the beam coupling in to the fundamental mode in the waveguide, the focus diameter was adjusted to 160μm at the capillary entrance, corresponding to 64.3% of the bore diameter [22]. The output beam was collimated by the second lens $(f = 1m)$ and sent to a set of chirped mirrors $(-2800\ \mathrm{fs}^2)$ to compensate the dispersion of the spectrally broadened pulses , and finetuning of the dispersion compensation was achieved by delicately adjusting the gas pressure.

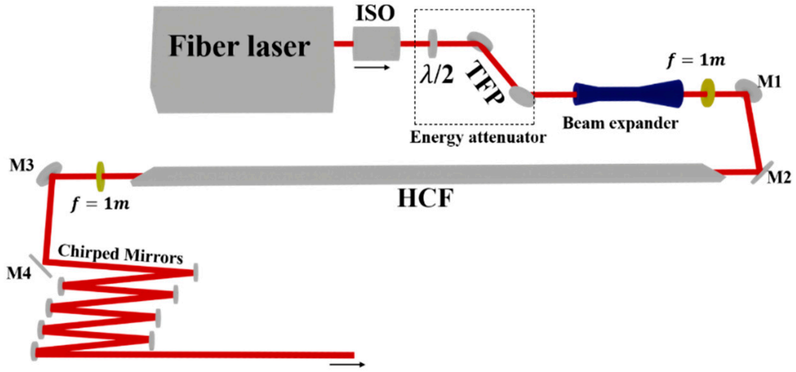

Figure 1. Schematic layout of the HCF post-compression module. ISO: optical isolator; λ/2: half-waveplate; TFP: thin-film polarizer; M1, M2: fine-tuning mirrors; HCF: hollow-core fiber; CM: chirped mirrors ($-2800\ \mathrm{fs}^2$).

The Herriott-type MPC configuration is schematically shown in Figure 2. Following a similar beam conditioning procedure as for the HCF system, the optimized beam was coupled into the MPC using a lens with a focal length of 1 m and a pair of fine-tuning mirrors (M1 and M2). Inside the MPC chamber, two 2-inch concave mirrors with a radius of curvature (ROC) of 300 mm are mounted, along with a manual translation stage, two pick-up mirrors, and gas inlet ports. The chamber was filled with argon at a backing pressure of 4.2 bar to provide sufficient nonlinearity for spectral broadening via self-phase modulation.

To maximize propagation efficiency and minimize the impact of group delay dispersion (GDD), all mirrors were coated with high-reflectivity layers (>99.9%) and exhibited minimal GDD (<20 fs²) over the 950–1130 nm spectral range. The translation stage allows precise adjustment of the distance between the two concave mirrors, which was set to 334 mm. Beam coupling into and out of the MPC chamber was achieved using two small rectangular flat pick-up mirrors positioned close to the concave cavity mirrors. The beam undergoes 28 reflections on each concave mirror, resulting in a total beam path length of approximately 19 m within the MPC cavity.

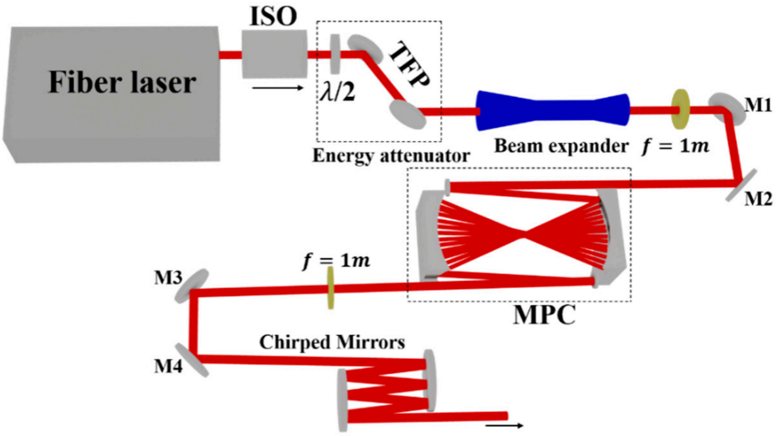

Figure 2. Schematic layout of the MPC post-compression module. The beam is coupled into the Herriott-type multi-pass cell using a beam expander and a lens (f = 1 m) and fine-tuning mirrors (M1, M2). The output is collimated and compressed by chirped mirrors (−3000 fs²).

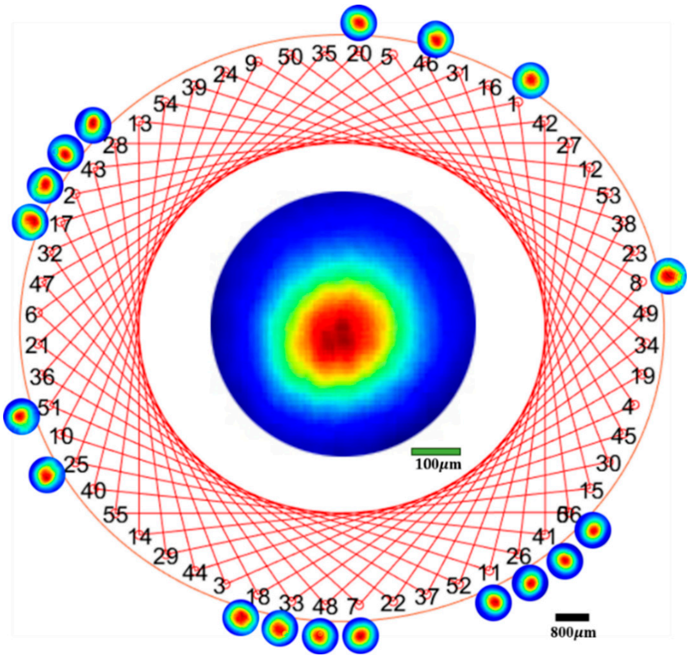

Figure 3. Simulated beam path and measured beam profiles at the MPC cavity center (middle image) and behind the cavity mirrors for different roundtrips.

After fine adjustment of the beam coupling into the cavity mode, the ray bundle forms a circular pattern on the concave mirrors, as shown in Figure 3. The beam waist at the cavity center was measured to be 442 µm (diameter at 1/e²), expanding to 660 µm on the cavity mirror surfaces. The beam waist at various round trips was characterized by placing a camera 85 mm behind the cavity mirror. As demonstrated in Figure 3, the beam waist is evenly distributed on the cavity mirrors across different round trips, indicating that the beam has been adequately coupled into the cavity mode.

The output beam from the MPC was collimated by a lens with a focal length of 1 m before being sent to a pair of chirped mirrors. Each chirped mirror provides a GDD of −500 fs². Since the beam diameter was only 3 mm, three reflections on each mirror were arranged to achieve a total dispersion compensation of −3000 fs². The final post-compressed pulse duration was measured using a commercial autocorrelator (Pulsecheck NX 50, APE).

The cascaded compression scheme is sketched in Figure 4, which follows a similar configuration to that reported in the literature [23], we employed a second Yb-doped fiber laser (100 kHz, 440 μJ, 223 fs, central wavelength 1030 nm) as the driving source. the output beam firstly passes through an optical isolator to prevent back-reflections. A motorized energy attenuator consisting of a half-waveplate and two thin-film polarizers is installed after the isolator for precise pulse energy control. A flexible beam expander and a focal lens (f = 1 m) are then used to adjust the beam waist for optimal coupling into the first compression stage.

The first stage of the cascaded system is a Herriott-type multi-pass cell. The MPC consists of two 2-inch concave mirrors with a radius of curvature of 300 mm, separated by 385 mm. The beam undergoes 34 round trips (68 reflections) with a total path length of approximately 26.2 m. The MPC chamber is filled with 1 bar argon as the nonlinear medium. All mirrors have high reflectivity (>99.9%) and minimal group delay dispersion (<20 fs²) over the 950–1130 nm spectral range. The output beam from the MPC is collimated and compressed using a pair of chirped mirrors providing −400 fs² dispersion compensation, yielding 32 fs pulses with a transmission efficiency of 96%.

The second stage of the cascaded system is a hollow-core fiber compression module. The output from the MPC is coupled into an HCF of 1 m length with an inner diameter of 400 μm. The HCF is housed in a vacuum chamber filled with 1 bar xenon gas. The beam waist at the fiber entrance is carefully adjusted to 64.3% of the bore diameter to optimize fundamental mode coupling. The output from the HCF is collimated and sent to two pairs of chirped mirrors (Ultrafast Innovation) providing a total dispersion compensation of −240 fs² over the 650–1350 nm spectral range.

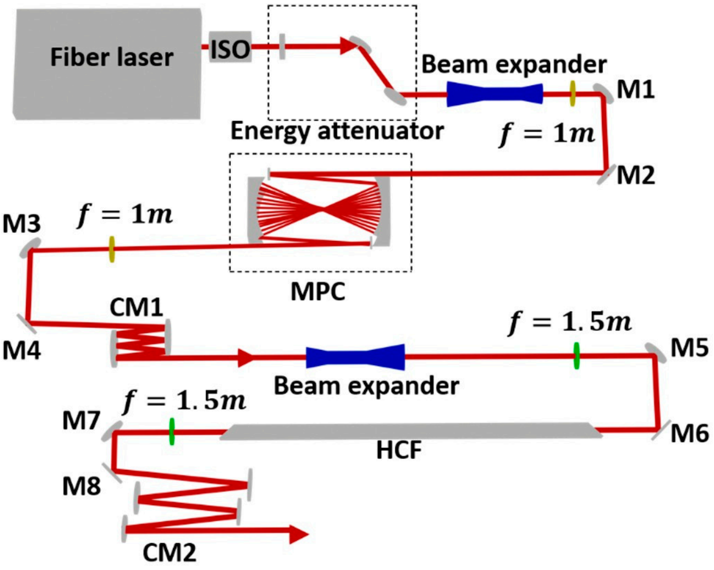

Figure 4. Cascade MPC and HCF post-compression setup.

3. Results

3.1. Post-Compression Results with HCF Module

With the HCF post-compression module, the input Gaussian beam was successfully coupled into the fundamental mode of the argon-filled capillary. The transmission efficiency as a function of input power was investigated, as shown in Figure 5. Each error bar represents the standard deviation over 10 consecutive measurements. The transmission efficiency exhibits a trend of initially increasing with input power, reaching a maximum coupling efficiency of approximately 56% at an input power of around 20 W, before decreasing to 54% when the input power was increased to 65.2 W. The initial increase is attributed to improved mode matching, where moderate self-focusing reduces beam divergence and enhances overlap with the fundamental EH_{11} mode. At higher input power, however, strong nonlinear effects—particularly the interplay between Kerr self-focusing and plasma-induced defocusing—lead to focal instability and spatiotemporal distortions. These effects promote coupling into higher-order modes with larger propagation losses, thereby reducing the overall efficiency.

In addition, the coupling efficiency is sensitive to the input wavefront quality. Residual aberrations degrade the overlap with the fundamental mode, consistent with the wavefront evolution observed in Figure 8. Combined with gas-related losses and practical system imperfections, these factors explain the lower efficiency (~55%) compared to optimized HCF systems (~70%), highlighting the critical role of spatial phase and nonlinear dynamics in HCF-based post-compression.

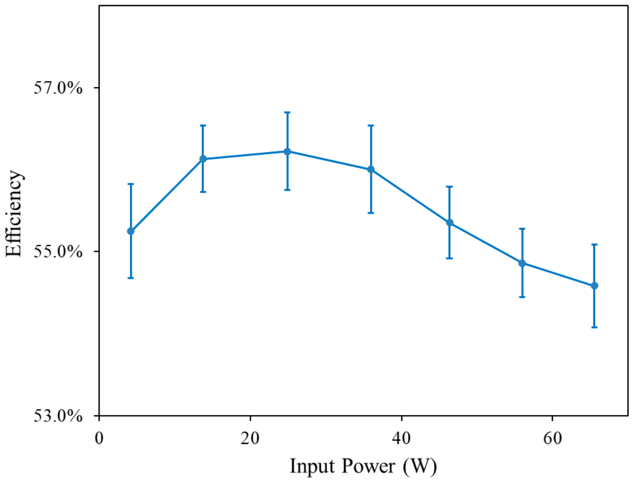

Figure 5. Measured HCF transmission efficiency as a function of input power.

The spectral broadening dynamics within the gas-filled HCF are governed by the accumulated nonlinear phase shift, i.e., the B-integral, defined as $B = \frac{2\pi}{\lambda} n_2 I_0 L_{\text{eff}}$, which arises from SPM. As shown in Figure 6a, the output spectral bandwidth increases monotonically with input power, consistent with the linear scaling of B (and thus the maximum frequency shift $\Delta\omega_{\max}$) with peak intensity I_0. Given that SPM is the dominant mechanism for spectral expansion, the gas pressure exerts an influence comparable to that of the input power by modulating the nonlinear refractive index n_2, which is linearly proportional to the gas density. This is demonstrated in Figure 6b, which presents the output spectra measured under argon pressures of 3, 5, and 7 bar using the same high-resolution spectrometer (FX 2000, Zolix) as in Figure 6a. A clear progressive spectral broadening is observed with increasing pressure, following the scaling $\Delta\omega \propto n_2 \propto P$ at a fixed input power. However, it should be noted that while higher pressure enhances spectral broadening, it also increases the risk of ionization-induced losses and plasma defocusing. Therefore, an optimal pressure exists that balances spectral broadening against nonlinear propagation stability. These results collectively underscore the critical role of pressure-mediated $n_2$tuning in optimizing HCF-based pulse compressors.

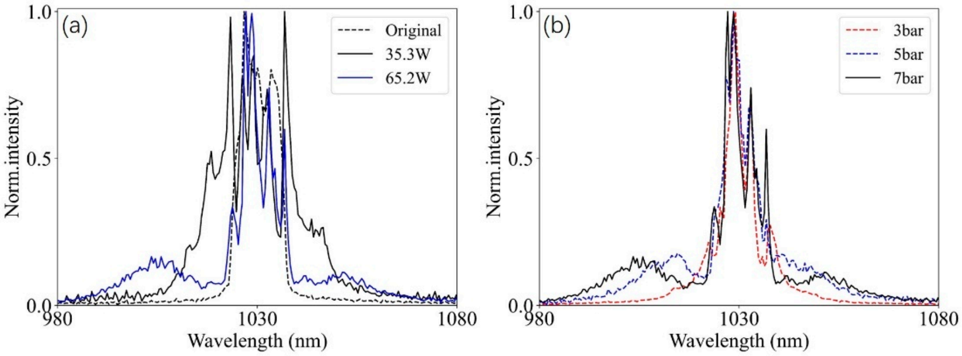

Figure 6. Measured output beam spectra with different input power and different gas pressures to HCF: (a) Spectral profiles of the original input pulse without gas (black dashed line), output spectra at input powers of 35.3 W (black solid line) and 65.2 W (blue solid line). (b) Spectral broadening characteristics under argon pressures of 3 bar (red dashed line), 5 bar (blue dotted line), and 7 bar (black solid line), measured at a constant input power of 65.2 W.

Under the argon backing pressure of 7 bar, the HCF output pulse exhibits a 75 nm spectral bandwidth at the −10 dB level, corresponding to a Fourier-transform-limited (FTL) pulse duration of 26.5 fs(red dashed line in Figure 7). Due to the nonlinear SPM process, the spectrally broadened pulse carries a significant amount of dispersion, which must be compensated to achieve pulse compression. A set of chirped mirrors providing a total GDD of −2800 fs² was employed for this purpose. The final compressed pulse duration was measured to be 27 fs (FWHM) using an autocorrelator, as shown in Figure 7(blue solid line). This result is in excellent agreement with the SPM-based numerical simulation (black dashed line in Figure 7), which was performed using the PyNLO package [24,25], confirming the effectiveness of the dispersion management strategy.

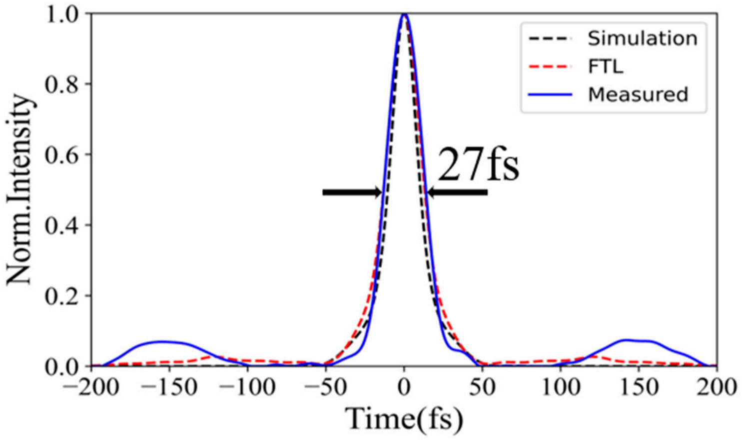

Figure 7. Temporal profiles of the HCF post-compressed beam with argon backing pressure at 7bar: (a) pulse from SPM-based simulation (black dotted line), (b) the FTL temporal profile of the broadened spectra (red dashed line), (c) measured temporal profile by autocorrelator (blue solid line).

A Shack-Hartmann wavefront sensor (HASO4 VIS, Imagine Optic) was used to inspect the beam spatial profile and wavefront quality. The sensor was pre-calibrated using a 1030 nm light source to ensure measurement accuracy. The beam spatial profiles and corresponding wavefront maps before and after the HCF module are presented in Figure 8 (left and right columns, respectively). After propagating through the 1.35-m-long HCF, the beam spatial distribution becomes noticeably more symmetrical, which is attributed to the waveguide effect. Quantitative wavefront analysis reveals a marked improvement in spatial phase quality: the peak-to-valley (PV) value decreases from 0.115λ to 0.095λ, and the root-mean-square (RMS) value decreases from 0.021λ to 0.015λ (where λ = 1030 nm). To identify the specific aberration components contributing to this improvement, Zernike polynomial decomposition was performed, as summarized in Table 1. Among the basic aberrations, including astigmatism (0° and 45°), coma (0° and 90°), and spherical aberration, the most significant improvement is observed in the 45° astigmatism component.

This wavefront originates from the mode-selective coupling process in the HCF. By optimizing the input beam waist to 64.3% of the bore diameter, the fundamental EH_{11} mode is preferentially excited, while higher-order modes are strongly suppressed due to their higher propagation losses. Consequently, the HCF exhibits inherent modal filtering properties, which effectively suppress higher-order modes and reduce low-order aberrations, leading to improved output beam quality. This result is consistent with the well-established mode-cleaning capability of hollow-core fibers and provides quantitative experimental evidence under high-power, high-repetition-rate operating conditions.

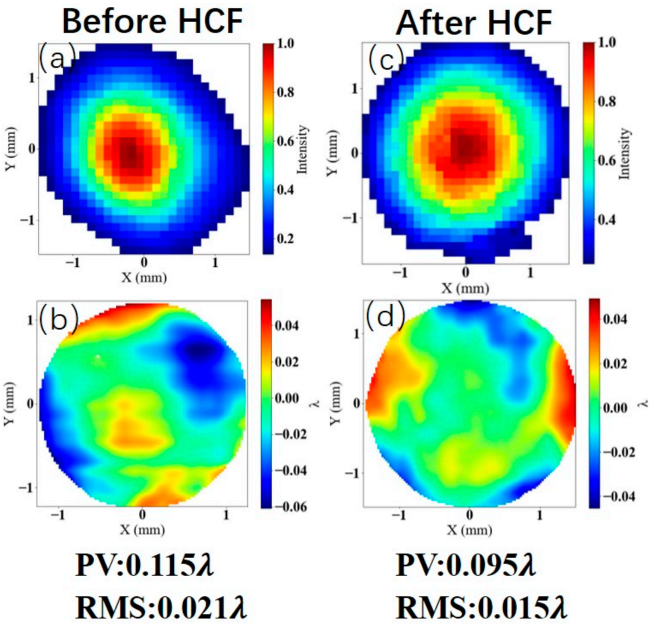

Figure 8. Beam profiles and wavefronts measured before and after the HCF module. (a) Beam profile before HCF compression; (b) wavefront map before HCF compression (PV = 0.28λ, RMS = 0.046λ); (c) beam profile after HCF compression; (d) wavefront map after HCF compression (PV = 0.14λ, RMS = 0.02λ).

Table 1. Zernike polynomials of the beam before and after the HCF module.

	Astigmatism 0°	Astigmatism 45°	Coma 0°	Coma 90°	Spherical
Before HCF(λ)	-0.012	-0.013	0.008	0.008	-0.007
After HCF(λ)	0.027	-0.008	0.007	0.011	-0.001

3.2. Post-Compression Results with MPC Module

Figure 9 shows the measured transmission efficiency of the MPC as a function of input power over the range of 5 W to 70 W. Each data point represents the average of ten consecutive measurements, and the error bars indicate the standard deviation. The MPC maintains a high transmission efficiency between 90% and 91% across the entire tested power range. A slight decrease from 91% at low power to 90% at the maximum input power of 66 W is observed, which is attributed to thermal effects induced by high-power operation that slightly alter the mode-matching condition within the cavity. This relatively stable efficiency demonstrates the good power-handling capability of the MPC scheme.

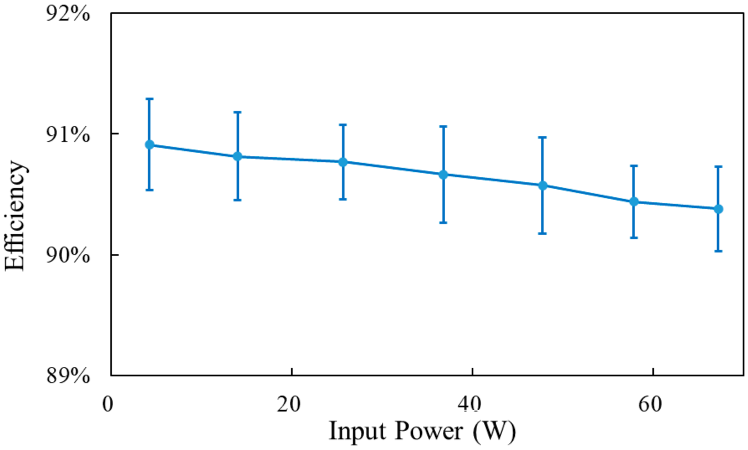

Figure 9. Transmission efficiency of the MPC as a function of input power measured under 4.2 bar argon. Error bars represent the standard deviation over ten consecutive measurements.

The spectral broadening and subsequent pulse compression performance of the MPC were characterized under an argon pressure of 4.2 bar. The 230 fs input pulses underwent SPM during 56 reflections (28 round trips) within the Herriott-type cavity, resulting in significant spectral broadening. The output spectrum, shown in Figure 10a, exhibits a −10 dB bandwidth of approximately 70 nm, which supports a Fourier-transform-limited pulse duration of 33 fs. To compensate the dispersion accumulated during nonlinear propagation, a pair of chirped mirrors providing a total group delay dispersion of −3000 fs² was employed. The compressed pulse duration was measured to be 34 fs (FWHM) using an autocorrelator, assuming a Lorentz pulse shape for fitting, as presented in Figure 10b. Numerical simulations were performed using the generalized nonlinear Schrödinger equation, taking into account the gas pressure, cavity geometry, and mirror dispersion. The simulated spectrum and temporal profile are shown in Figure 10c and Figure 10d, respectively. The experimental results show good agreement with the simulations in terms of both spectral shape and compressed pulse duration, with the slight discrepancy in the spectral asymmetry attributed to higher-order nonlinear effects such as self-steepening, which are not fully captured in the simplified model.

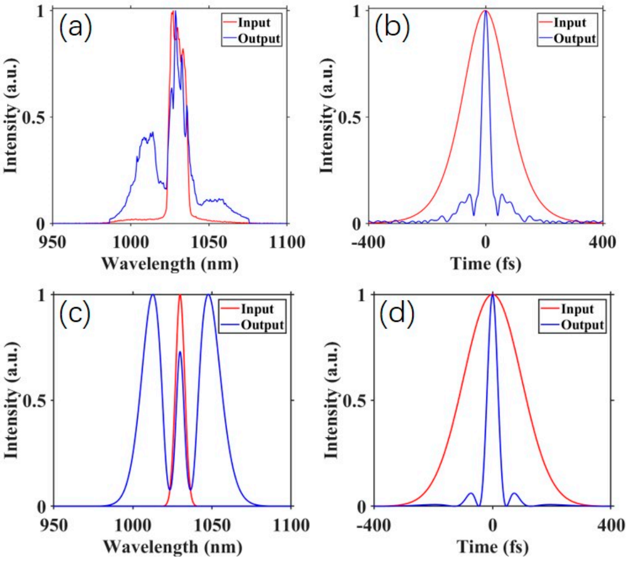

Figure 10. Experiment (upper row) and simulation (lower row) spectrum (left column) and temporal (right column) profiles for MPC module. (a) Measured input spectrum(red) and output spectrum(blue), (b) Temporal profile measured at the laser output (red) and after MPC (blue), (c) Spectrum on MPC input(red), spectrum after MPC (blue) in the simulation, (d) Temporal profile at MPC input (red) and output (blue) in the simulation.

The spatial properties of the beam were rigorously characterized before and after the MPC (see Figure 11) using the same Shack–Hartmann wavefront sensor. In contrast to the HCF, which improves beam quality through waveguide modal filtering, the MPC exhibits a distinct spatial evolution characteristic. Despite having a significantly poorer input wavefront (PV = 2.319λ, RMS = 0.322λ), the output wavefront shows substantial improvement after passing through the MPC module, with PV reduced to 0.573λ and RMS reduced to 0.094λ. Further analysis of the Zernike polynomials (Table 2) reveals the detailed evolution of individual aberration components, particularly a notable reduction in the 45° astigmatism component from 0.806λ to −0.106λ, as well as reductions in coma and spherical aberration.

This observed wavefront improvement is attributed to the quasi-waveguide mode-filtering effect of the Herriott-type MPC. In an ideal MPC with perfectly aligned spherical mirrors, the cavity supports a set of eigenmodes that can propagate stably over many round trips. Under proper mode-matching conditions, higher-order transverse modes experience larger diffraction losses due to their greater divergence angles and are effectively filtered out during multiple reflections, while the fundamental mode achieves self-reproduction and propagates with low loss. This quasi-waveguide effect endows the MPC with mode-cleaning capabilities similar to those of the HCF, leading to improved output beam quality.

However, the MPC's wavefront improvement is highly dependent on the input beam mode-matching accuracy and cavity alignment. While the quasi-waveguide effect filters out higher-order spatial modes, low-order aberrations such as astigmatism that are already present in the input beam or introduced by residual surface errors of the concave mirrors can still persist or be modified through the cavity propagation. In our experiment, the residual output aberrations (PV = 0.573λ, primarily 45° astigmatism) are likely contributed by a combination of factors: (i) the significantly poorer input wavefront (2.319λ) compared to the HCF case (0.115λ); (ii) minor residual surface figure errors of the concave mirrors; and (iii) slight misalignment from the ideal cavity condition. Unlike the HCF waveguide, which directly constrains transverse modes through boundary conditions and is relatively tolerant to input aberrations, the MPC's quasi-waveguide filtering effect requires precise mode matching to achieve optimal performance. This sensitivity explains why the output wavefront of the MPC (0.573λ), despite substantial improvement from its input, remains worse than that of the HCF output (0.095λ), which benefits from both excellent input beam quality and strong waveguide modal filtering.

It is also worth noting that the MPC's transmission efficiency remains high (90–91%) across the tested power range, and the wavefront improvement is consistently observed under proper operating conditions. These results demonstrate that the MPC, when properly aligned and mode-matched, can serve as an effective beam-cleaning element in high-power post-compression systems, although its performance is more sensitive to input conditions compared to the HCF.

Table 2. Zernike polynomials of the beam before and after the MPC module.

	Astigmatism 0°	**Astigmatism 45°**	**Coma 0°**	**Coma 90°**	**Spherical**
Before MPC(λ)	-0.353	0.806	0.058	0.113	0.022
After MPC(λ)	0.205	-0.106	0.010	0.026	-0.005

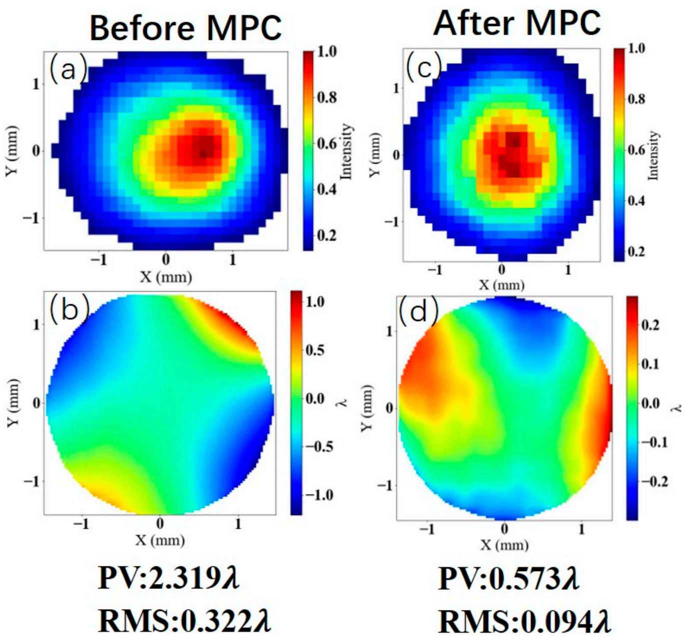

Figure 11. Beam profiles and wavefronts measured before and after the MPC module. (a) Beam profile before MPC compression; (b) wavefront map before MPC compression (PV = 2.319λ, RMS = 0.322λ); (c) beam profile after MPC compression; (d) wavefront map after MPC compression (PV = 0.573λ, RMS = 0.094λ).

3.3. Post-Compression Results with Cascade Compression Module

The measured spectral intensity and temporal profile at the output of this first-stage MPC are shown in Figure 12a and Figure 12b, respectively. As presented in Figure 12a, the output spectrum exhibits a −10 dB bandwidth of approximately 72 nm, which supports a Fourier-transform-limited pulse duration of about 30 fs. After dispersion compensation using chirped mirrors providing a total group delay dispersion of −400 fs², the pulse duration was measured to be 32 fs (FWHM) using an autocorrelator, assuming a sech² pulse shape for fitting, as shown in Figure 12b. The measured pulse duration is close to the Fourier-transform limit, indicating efficient dispersion compensation. The transmission efficiency of this first-stage MPC was measured to be 96%. This efficiency improvement was primarily contributed by the lower gas pressure, which reduces scattering and ionization losses.

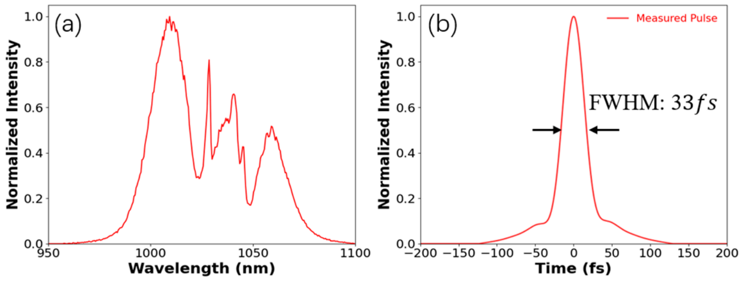

Figure 12. Measured spectral intensity (a) and temporal profile (b) at the output of the first-stage MPC in the cascaded compression scheme.

The measured spectral intensity and temporal profile at the output of this second-stage HCF are shown in Figure 13a and Figure 13b, respectively. As presented in Figure 13a, the output spectrum exhibits a broad bandwidth spanning from approximately 700 nm to 1200 nm, supporting a Fourier-transform-limited (FTL) pulse duration of 7.4 fs. After dispersion compensation using two pairs of chirped mirrors (Ultrafast Innovation) providing a total group delay dispersion of −240 fs² over the 650–1350 nm spectral range, the pulse duration was measured to be 7.5 fs (FWHM) using an autocorrelator, assuming a sech² pulse shape for fitting, as shown in Figure 13b. The measured pulse duration is very close to the Fourier-transform limit, indicating near-ideal dispersion compensation.

The transmission efficiency of this second-stage HCF was measured to be 72.5%, and the overall transmission efficiency of the cascaded system from the second laser input to the final output is approximately 70%.

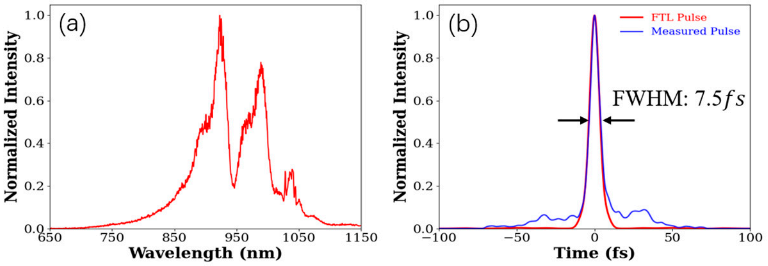

Figure 13. Measured spectral intensity (a) and temporal profile (b) at the output of the second-stage HCF in the cascaded compression scheme.

The spatial beam quality at each stage of the cascaded compression scheme was characterized using a quadri-wave lateral shearing interferometer (QWLSI) wavefront sensor (SID4, PHASICS). A key advantage of this sensor is its achromatic operation over the 400–1100 nm spectral range, which eliminates the need for recalibration when measuring different wavelengths.

The beam profiles and corresponding wavefront maps before and after the first-stage MPC [Figure 14a–d] and before and after the second-stage HCF [Figure 14e–h] are presented in Figure 14.

Before entering the cascaded compression system, the driving laser exhibits an excellent initial beam quality, with a wavefront PV of approximately 0.002λ and RMS of approximately 0.001λ (λ = 1030 nm). After propagating through the first-stage MPC (1 bar Ar, 34 round trips), the output beam wavefront remains nearly unchanged, with PV and RMS values of 0.002λ and 0.001λ, respectively, as shown in Figure 14c,d. This indicates that under proper mode-matching and low-pressure conditions, the MPC introduces negligible additional aberrations while achieving a compression factor of approximately 7 (from 223 fs to 32 fs).

The output beam from the first-stage MPC is then coupled into the second-stage HCF (1 m, 400 μm inner diameter, 1 bar Xe). After propagation through the HCF and subsequent dispersion compensation, the beam quality remains excellent, as shown in Figure 14g,h. The wavefront PV and RMS values are measured to be 0.002λ and 0.001λ, respectively, which are almost identical to those of the input beam. This result demonstrates that the HCF, under proper coupling conditions, preserves the spatial coherence of the beam while further compressing the pulse from 32 fs to 7.5 fs with a transmission efficiency of 72.5%.

Overall, the cascaded MPC–HCF scheme achieves a total compression factor of approximately 30 (from 223 fs to 7.5 fs) with an overall transmission efficiency of approximately 70%, while maintaining excellent wavefront quality throughout the entire system (PV ≤ 0.002λ, RMS ≤ 0.001λ), as measured by the SID4 QWLSI wavefront sensor.

Table 3. Zernike polynomials of the beam before and after the Cascade module.

	Astigmatism 0°	Astigmatism 45°	Coma 0°	Coma 90°	Spherical
Before MPC(λ)	-0.002	-0.001	-0.000	0.000	0.001
After MPC(λ)	-0.002	0.002	0.000	-0.000	0.001
Before HCF(λ)	0.003	0.000	0.002	0.002	0.001
After HCF(λ)	-0.002	0.004	-0.000	-0.001	0.000

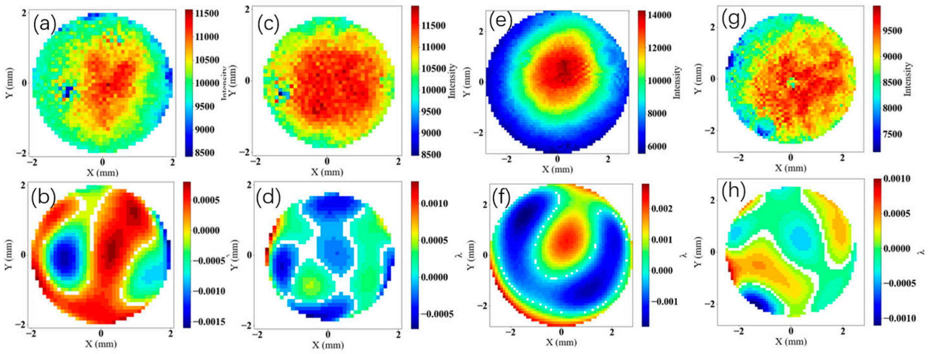

PV:0.002λ **RMS:0.001λ** **PV:0.002λ** **RMS:0.001λ** **PV:0.005λ** **RMS:0.001λ** **PV:0.002λ** **RMS:0.001λ**

Figure 14. Beam profiles and wavefronts measured at each stage of the cascaded compression scheme. (a) Beam profile before MPC compression; (b) wavefront before MPC compression; (c) beam profile after MPC compression; (d) wavefront after MPC compression; (e) beam profile before HCF compression; (f) wavefront before HCF compression; (g) beam profile after HCF compression; (h) wavefront after HCF compression.

3.4. Experimental Results of HHG with Different Driving Beam Conditions

The beam quality directly impacts HHG photon flux by influencing the phase-matching conditions and focal spot profile. An ideal plane-like wavefront is crucial for maintaining a long and stable interaction region between the driving laser and the generation medium, ensuring constructive interference of the emitted harmonics along the propagation direction. Aberrations such as astigmatism in the driving beam can disrupt this coherence, effectively shortening the useful interaction length and reducing the harmonic conversion efficiency [26].

To evaluate the impact of beam quality on HHG, we performed experiments using the compressed pulses from both the HCF and the MPC under nominally similar conditions. The HHG setup followed our previous work [27]. In both cases, the beam was focused by an f = 200 mm lens into an argon gas jet. For the HCF-driven case, the pulse energy at the target was 137.5 μJ with a duration of 27 fs at 200 kHz repetition rate, and the argon backing pressure was set to 6.5 bar. For the MPC-driven case, the pulse energy was 295 μJ with a duration of 34 fs at 200 kHz, and the argon backing pressure was 6.0 bar. The photon flux was calculated using a calibrated XUV photodiode (AXUV100G, Opto Diode) with corrections for the grating efficiency and Al filter transmittance

As shown in Figure 15a, the HCF-driven source produced a well-resolved harmonic spectrum spanning from 25 nm to 40 nm (H25–H41 of the 1030 nm driver), with the strongest harmonic at approximately 30 nm and a photon flux of 1.25×10^{11} photons/s. The MPC-driven source produced a similar spectral range but with a lower photon flux of 4.95×10^{10} photons/s (Figure 15b), approximately 2.5 times lower than that achieved with the HCF driver, despite the MPC pulses having higher single-pulse energy (295 μJ vs. 137.5 μJ).

Several factors may contribute to this difference. First, the pulse duration is shorter for the HCF driver (27 fs vs. 34 fs), which, according to literature scaling laws [28], would enhance HHG efficiency by a factor of approximately 1.3–1.5. Second, the HCF driver has a significantly better output wavefront quality (PV = 0.095λ vs. 0.573λ for the MPC), which improves phase matching and focal spot quality. Third, the higher pulse energy of the MPC driver (by a factor of ~2.1) would, in isolation, favor higher HHG yield. Taking these factors together, the observed 2.5× advantage of the HCF driver cannot be explained by pulse duration or pulse energy alone, strongly suggesting that wavefront quality plays a significant role in determining HHG photon flux.

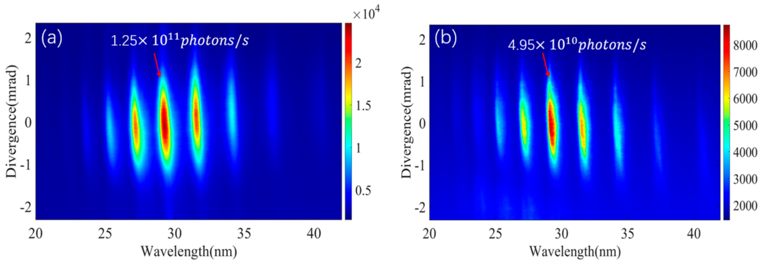

Figure 15. XUV spectra argon driven by HCF- and MPC- compressed pulses. (a) 6.5 bar backing pressure argon driven by 137.5 μJ, 27 fs pulse from HCF; (b) 6.0 bar backing pressure argon driven by 295 μJ, 34 fs pulse from MPC.

5. Conclusions

In this work, we have experimentally compared the temporal and spatial properties of post-compressed pulses using HCF and MPC schemes under identical driving conditions (230 fs, 200 kHz). The HCF compresses pulses to 27 fs (efficiency ~55%) and improves beam quality through modal filtering (PV from 0.115λ to 0.095λ). The MPC compresses pulses to 34 fs (efficiency ~90%) and exhibits a quasi-waveguide mode-filtering effect, substantially improving output wavefront quality (PV from 2.319λ to 0.573λ) despite a poorer input.

Using a second Yb-fiber laser (223 fs, 100 kHz), a cascaded MPC–HCF scheme generates 7.5 fs pulses with ~70% overall efficiency while maintaining excellent wavefront quality (PV ~0.002λ, RMS ~0.001λ).

Both single-post-compressed sources were subsequently employed to drive HHG, producing bright XUV radiation within the 25–40 nm spectral range. HHG experiments show that the HCF-driven source produces ~2.5 times higher photon flux (1.25×10^{11} vs. 4.95×10^{10} photons/s) than the MPC-driven source, despite lower pulse energy. This difference cannot be fully explained by pulse duration or energy alone, indicating that wavefront quality plays a significant role in HHG efficiency.

These results demonstrate that spatial phase evolution is a critical parameter in post-compression design and should be considered alongside temporal compression and efficiency for phase-sensitive applications such as HHG. Furthermore, by incorporating adaptive optics to pre-compensate the driving laser wavefront, the spatial properties of the XUV beam can be actively tailored and enhanced, opening pathways toward high brightness, fully coherent XUV sources for advanced applications in nanoscale imaging and metrology.

Institutional Review Board Statement: Not applicable.

Data Availability Statement: Data underlying the results presented in this paper are not publicly available at this time but may be obtained from the authors upon reasonable request.

Acknowledgments: Natural Science Foundation of Top Talent of SZTU(GDRC202325, GDRC202528), National Key R&D Program of China (2024YFA1612103,2024YFA1612104), Natural Science Foundation of China (12505274,12575260,12205203,12404312), Guangdong Province Key Construction Discipline Scientific Research Capacity Improvement Project (2021ZDJS107), Guangdong Basic and Applied Basic Research Foundation (2414050002917).

Conflicts of Interest: The authors declare no conflicts of interest.

Abbreviations

The following abbreviations are used in this manuscript:

HCF	Hollow core fiber
MPC	Multi pass cell
HHG	High harmonic generation
SPM	Self-phase modulation

CPA	Chirped pulse amplification
XUV	Extreme ultraviolet

References

1. Strickland D, Mourou G. Compression of amplified chirped optical pulses. Optics communications, 1985, 55(6): 447-449.
2. Zhang Z, Wu F, Hu J, et al. The laser beamline in SULF facility, High Power Laser Science and Engineering, 2020, 8(4): 01-07.
3. Brown D C. Ultrahigh-average-power diode-pumped Nd: YAG and Yb: YAG lasers. IEEE Journal of Quantum Electronics, 2002, 33(5): 861-873.
4. Brons J, Pervak V, Bauer D, et al. Powerful 100-fs-scale Kerr-lens mode-locked thin-disk oscillator. Optics Letters, 2016, 41(15): 3567-3570.
5. Schulz M, Riedel R, Willner A, et al. Yb: YAG Innoslab amplifier: efficient high repetition rate subpicosecond pumping system for optical parametric chirped pulse amplification. Optics letters, 2011, 36(13): 2456-2458.
6. Müller M, Kienel M, Klenke A, et al. 1 kW 1 mJ eight-channel ultrafast fiber laser. Optics letters, 2016, 41(15): 3439-3442.
7. Sizhi Xu, Xing Liu, Yubo Gao, et al. Thin-disk multi-pass amplifier for kilowatt-class ultrafast lasers.High Power Laser Science and Engineering,2024,12(5):22-27
8. Heyl C M, Arnold C L, Couairon A, et al. Introduction to macroscopic power scaling principles for high-order harmonic generation. Journal of Physics B: Atomic, Molecular and Optical Physics, 2016, 50(1): 013001.
9. Lorek E, Larsen E W, Heyl C M, et al. High-order harmonic generation using a high-repetition-rate turnkey laser. Review of Scientific Instruments, 2014, 85(12).
10. Chen X, Jullien A, Malvache A, et al. Generation of 4.3 fs, 1 mJ laser pulses via compression of circularly polarized pulses in a gas-filled hollow-core fiber. Optics letters, 2009, 34(10): 1588-1590.
11. Böhle F, Kretschmar M, Jullien A, et al. Compression of CEP-stable multi-mJ laser pulses down to 4 fs in long hollow fibers. Laser Physics Letters, 2014, 11(9): 095401.
12. Nagy T, Kretschmar M, Vrakking M J J, et al. Generation of above-terawatt 1.5-cycle visible pulses at 1 kHz by post-compression in a hollow fiber. Optics Letters, 2020, 45(12): 3313-3316.
13. Daniault L, Kaur J, Gallé G, et al. Sub-2-cycle post-compression of multi-mJ energy Ti: sapphire laser pulses in a gas-filled multi-pass cell. Optics Letters, 2024, 49(23): 6833-6836.
14. Lu C H, Wu W H, Kuo S H, et al. Greater than 50 times compression of 1030 nm Yb: KGW laser pulses to single-cycle duration. Optics express, 2019, 27(11): 15638-15648.
15. Liu Y, Fang S. Single-cycle pulse compression with over 20-fold peak power enhancement at an average power of 13.5 W. Optics Letters, 2025, 50(17): 5482-5485.
16. Pi Z, Kim H Y, Goulielmakis E. Synthesis of single-cycle pulses based on a Yb: KGW laser amplifier. Optica, 2025, 12(3): 296-301.
17. Plach M, Vismarra F, Appi E, et al. Spatial aberrations in high-order harmonic generation[J]. Ultrafast Science, 2024, 4: 0054.
18. Wodzinski T, Künzel S, Koliyadu J C P, et al. High-harmonic generation wave front dependence on a driving infrared wave front[J]. Applied optics, 2020, 59(5): 1363-1370.
19. Du Y, Li K, Niu J, et al. Multicolor wavefront sensing using Talbot effect for high-order harmonic generation[J]. Physical Review Research, 2024, 6(4): 043072.
20. Liu X, Pelekanidis A, Du M, et al. Observation of chromatic effects in high-order harmonic generation[J]. Physical Review Research, 2023, 5(4): 043100.
21. Balasubramaniam G M, Allam S R, Anand V, et al. Roadmap on singular optics and its applications[J]. Applied Physics B, 2026, 132(5): 58.
22. Abrams R. Coupling losses in hollow waveguide laser resonators. IEEE Journal of Quantum Electronics, 2003, 8(11): 838-843.

23. Lavenu, L.Natile, M.Guichard, F. , et al.High-power two-cycle ultrafast source based on hybrid nonlinear compression[J].Optics Express,2019,27,(3):1958-1967.DOI:10.1364/OE.27.001958.
24. Hult J. A fourth-order Runge–Kutta in the interaction picture method for simulating supercontinuum generation in optical fibers[J]. Journal of lightwave technology, 2007, 25(12): 3770-3775.
25. pyNLO developers. PyNLO: A Python package for nonlinear optics modeling. Available online: https://github.com/pyNLO/PyNLO
26. Marius Plach,Federico Vismarra,Elisa Appi , et al.Spatial Aberrations in High-Order Harmonic Generation[J].Ultrafast Science,2024,4,(1):35-43.DOI:10.34133/ultrafastscience.0054.
27. Jiatai Yao, Jiayue Liu, Jinxu Du, et al. Development of High-Photon-Flux Ultrafast Coherent Extreme-Ultraviolet Light Source Based on Gas High Harmonic Generation. Chinese Journal of Lasers, 2024, 51(19): 1901016.
28. Haedrich, Steffen,Rothhardt, Jan,Krebs, Manuel , et al.Single-pass high harmonic generation at high repetition rate and photon flux[J].Journal of Physics B: Atomic, Molecular and Optical Physics,2016,49,(17)DOI:10.1088/0953-4075/49/17/172002.